

Observation of Spin Hall Effect in Weyl Semimetal WTe₂ at Room Temperature

Bing Zhao^{1,2}, Dmitrii Khokhriakov², Yang Zhang³, Huixia Fu⁴, Bogdan Karpiak², Anamul Md. Hoque²,
Xiaoguang Xu¹, Yong Jiang¹, Binghai Yan⁴, Saroj P. Dash^{2,5,*}

¹*Beijing Advanced Innovation Center for Materials Genome Engineering, School of Materials Science and Engineering,
University of Science and Technology Beijing, Beijing 100083, China*

²*Department of Microtechnology and Nanoscience, Chalmers University of Technology, SE-41296, Göteborg, Sweden*

³*Max Planck Institute for Chemical Physics of Solids, 01187 Dresden, Germany*

⁴*Department of Condensed Matter Physics, Weizmann Institute of Science, Rehovot 7610001, Israel*

⁵*Graphene Center, Chalmers University of Technology, SE-41296 Göteborg, Sweden.*

Abstract

Discovery of topological Weyl semimetals has revealed the opportunities to realize several extraordinary physical phenomena in condensed matter physics. Specifically, these semimetals with strong spin-orbit coupling, broken inversion symmetry and novel spin texture are predicted to exhibit a large spin Hall effect that can efficiently convert the charge current to a spin current. Here we report the direct experimental observation of a large spin Hall and inverse spin Hall effects in Weyl semimetal WTe₂ at room temperature obeying Onsager reciprocity relation. We demonstrate the detection of the pure spin current generated by spin Hall phenomenon in WTe₂ by making van der Waals heterostructures with graphene, taking advantage of its long spin coherence length and spin transmission at the heterostructure interface. These experimental findings well supported by ab initio calculations show a large charge-spin conversion efficiency in WTe₂; which can pave the way for utilization of spin-orbit induced phenomena in spintronic memory and logic circuit architectures.

Keywords: Weyl semimetals, Spintronics, Spin Hall effect, Inverse Spin Hall effect, Graphene, van der Waals heterostructures, Rashba-Edelstein effect, 2D materials, TMDs, Spin transport, Gate-controlled.

Corresponding author: *Saroj P. Dash, Email: saroj.dash@chalmers.se

Department of Microtechnology and Nanoscience, Chalmers University of Technology, SE-41296, Göteborg, Sweden

Main

A strong resurgence of interest in two-dimensional (2D) transition metal dichalcogenide (TMD) is sparked with the successful preparation of materials with different properties that have the potential to revolutionize the future of electronics^{1,2}. While semiconducting TMDs brings enormous interest in transistors³⁻⁶ and optoelectronic applications⁷; the semimetals are predicted to host novel topological electronic states⁸⁻¹⁰. The recently predicted type-II Weyl semimetals¹⁰⁻¹² such as WTe_2 shows extraordinary electronic phenomena, like – a giant magnetoresistance¹³, high mobilities¹⁴, chiral anomaly¹⁵ and anomalous Hall effect¹⁶. These novel transport features indicate the existence of Weyl fermionic states, which are characterized by a tilted linear dispersion of Weyl cones and Fermi arc surface states. Due to the monopole-like Berry curvature in the momentum space, strong spin-orbit interaction, a unique spin texture in Weyl cones and Fermi arc surface states are predicted to exist¹⁷⁻¹⁹. In addition to the topological Weyl features in these semimetals, trivial spin-polarized Fermi arc surface states are also shown to exist at the Fermi level between the electron and the hole pockets at room temperature²⁰⁻²⁶. Taking advantage of these properties, recent experiments with WTe_2 /ferromagnet bilayers showed a control of spin-orbit torque arising from its crystal symmetry^{27,28}. Therefore, these 2D semimetals are considered to have a huge potential for ultra-low power spintronic devices²⁹ with an efficient conversion of charge-to-spin current, i.e. a large spin Hall effect (SHE) and (or) Rashba Edelstein effect (REE) at room temperature³⁰, however, it has not been yet experimentally measured.

Here, we report an observation of a large spin Hall effect (SHE) in semimetal WTe_2 devices at room temperature. We electrically detect the SHE signals by employing a van der Waals heterostructure device of WTe_2 and graphene, taking advantage of 2D layered structures of both classes of the materials. In these experiments, we exploit the best of both the worlds, such as a large spin Hall angle of WTe_2 , along with a long spin coherence length in graphene and an efficient spin transfer at the WTe_2 -graphene interface. The large charge-spin conversion signal stems mainly from bulk SHE of WTe_2 and possibly REE from the WTe_2 surface states. Our detailed spin sensitive electronic measurements both in the in-plane and perpendicular geometries, its angle and gate dependent studies, and theoretical calculations manifest the existence of the large spin Hall phenomena in WTe_2 devices at room temperature.

Results and Discussions

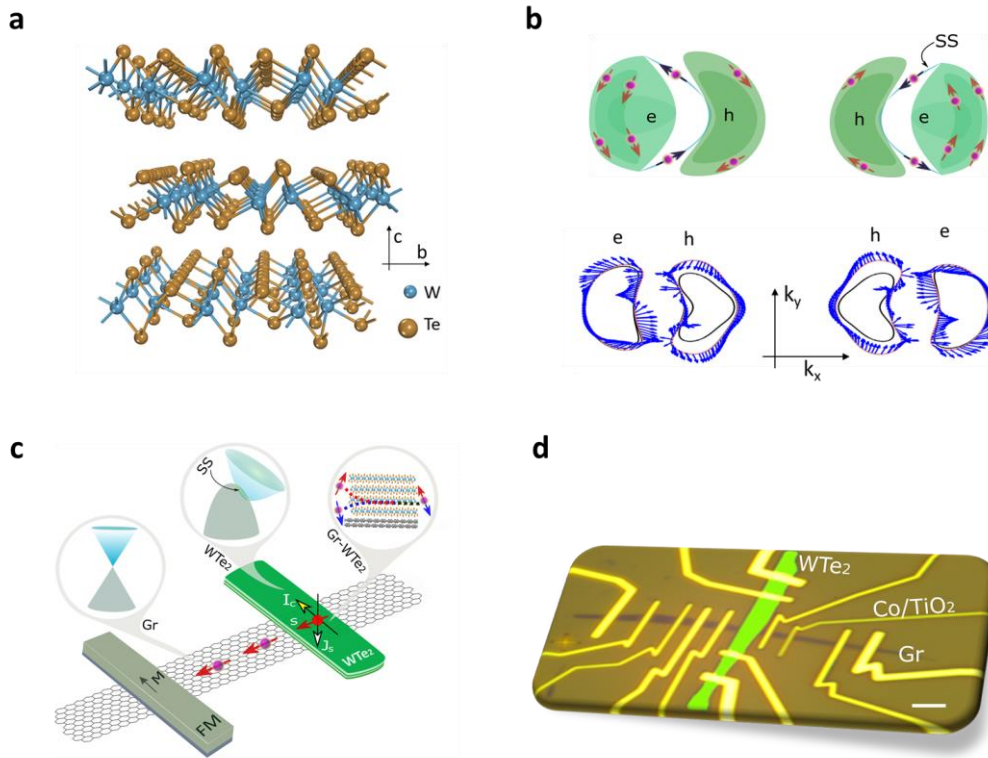


Figure 1. Scheme for detection of spin Hall effect and inverse spin Hall effect in WTe_2 . *a.* Crystal structure of the WTe_2 in T_d phase showing the layered nature. *b.* Top: schematic of the spin textures at the Fermi surface with the electron (e), hole (h) pockets and the surface states (SS). Bottom: the calculated electronic structure showing the coexistence of both the e and h pockets on the Fermi surface. Both the electron and hole bands split into two bands (red and black). The spin texture is indicated by blue arrows in one of the split bands (red). The two split bands have opposite directions of spin polarization. *c,d.* Schematics and colored optical microscope picture of a nanofabricated WTe_2 -graphene van der Waals heterostructure device with WTe_2 flake (green), ferromagnetic tunnel contacts of TiO_2/Co (FM) on the graphene (Gr) channel for the measurement of SHE and the ISHE on a SiO_2/Si substrate. The insets in the schematics show the band structures of the materials and the structure at the interface. The scale bar (white) in the device picture is $2\mu m$.

Figures 1a and 1b show the crystal structure and electronic structure, respectively, for WTe_2 in the T_d phase. At the Fermi surface, small electron and hole pockets coexist, demonstrating a compensating semi-metallic feature. Because of the inversion symmetry breaking and strong spin-orbit coupling (SOC), each pocket splits into two bands (see Fig. 1b). The Fermi surface exhibits a clear spin texture. The left and right parts of the Fermi surface and spin texture can be transformed into each other by a mirror reflection (k_x to $-k_x$). Such as strong spin-momentum locking feature indicates that the charge current comes together with a spin current, like SHE and REE. We experimentally investigated the influence of the spin degree of freedom on the charge currents and vice versa due to the presence of strong SOC, broken inversion symmetry and the novel spin textures in WTe_2 . The SHE in WTe_2 is expected to cause a transverse spin current induced by a charge current, whereas, the inverse SHE (ISHE) produces a transverse charge current that is caused by a pure spin current^{31,32}. Figure

1c,d show the nanofabricated devices consisting of van der Waals heterostructures of WTe_2 with few-layer graphene having ferromagnetic tunnel contacts to detect the SHE and ISHE in a spin sensitive potentiometric measurement (see Methods for details about the fabrication process). The heterostructure of graphene with WTe_2 flakes of 11-30 nm in thickness was used (from Hq Graphene), as measured by the atomic force microscope (AFM) (Supplementary Fig. S1). The quality of the WTe_2 was characterized by Raman spectrometer, showing peaks corresponding to the T_d -phase (Supplementary Fig. S2).

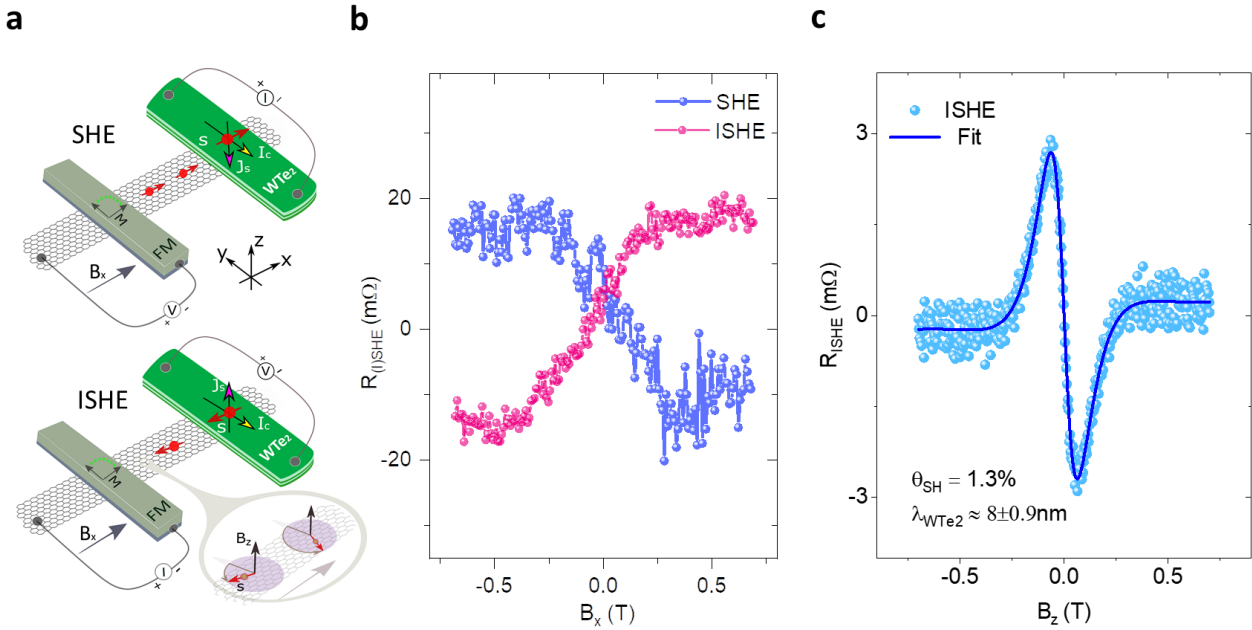


Figure 2. Electrical detection of spin Hall effect and Inverse spin Hall effect in WTe_2 at room temperature. **a.** Top: Schematic diagram of SHE measurement configuration, where a charge current in WTe_2 induces a spin current, which is injected and detected in graphene using a ferromagnetic contact in a non-local geometry, while the direction of the applied magnetic field sweep is B_x . Bottom: Schematic representation of ISHE measurement configuration, where a spin current injected from a ferromagnetic electrode into graphene enters the WTe_2 channel and hence induces a charge current giving rise to a voltage signal in WTe_2 , while the applied magnetic field sweeps along B_x and B_z , respectively. Inset is the out-of-plane B_z induced the spin precession. **b.** The change in SHE and ISHE resistance ($R_{(I)SHE} = V_{(I)SHE}/I$) with magnetic field B_x sweep due to the (I)SHE for bias currents of $+60 \mu A$ at room temperature for Dev 1 with channel length $L_{SHE} = 2.6 \mu m$ between Co and WTe_2 . **c.** ISHE signal data and fitting curve with out-of-plane magnetic field B_z in Dev 3 with channel length $L_{SHE} = 3.5 \mu m$ at bias currents of $+100 \mu A$. The ISHE signal data shown here were an average of 5 repeating measurement field sweeps. All the measurements were performed at 300K.

Figure 2a show the measurement geometries for SHE and ISHE in a hybrid device consisting of WTe_2 -graphene heterostructure and a ferromagnetic contact. The contact resistance of WTe_2 -graphene in the Dev 1 during SHE measurements was around $\sim 2k\Omega \cdot \mu m^2$ (Supplementary Fig. S3a). The application of longitudinal charge current (I) in WTe_2 produces a pure transverse spin current due to SHE, which is injected into the graphene at the interface and subsequently detected as a voltage

signal (V_{SHE}) by the non-local ferromagnetic Co tunnel contacts. The direction of the injected spins is in the plane of the graphene and perpendicular to the ferromagnet electrodes. The magnetic field B_x is applied perpendicular to the electrodes for changing the magnetization direction of Co from 90° to 0° with respect to the injected spins. Figure 2b shows the measured SHE data of $R_{\text{SHE}}=V_{\text{SHE}}/I$ for $I=60 \mu\text{A}$ at room temperature for a B_x sweep for Dev 1 with graphene channel length $L_{\text{SHE}}=2.6\mu\text{m}$. As expected, R_{SHE} follows a linear dependence at low B field, due to $\sin(\theta)$ dependence of the ferromagnetic moments rotation angle θ with the Co electrodes, whereas at large enough B field, the magnetization of Co rotates 90° and become parallel to B field and also the injected spin directions, resulting in the saturation of R_{SHE} .

Next, we performed the ISHE experiment, where a pure spin current is injected from the ferromagnet and absorbed by the WTe_2 . The spin current at the WTe_2 -graphene interface should give rise to a transversal charge voltage (V_{ISHE}) due to the ISHE (Fig. 2a). Figure 2b shows the measured ISHE data of $R_{\text{ISHE}}=V_{\text{ISHE}}/I$ for $I=60 \mu\text{A}$ at room temperature with $\sin(\theta)$ behavior for a B_x field sweep. These observed features confirm that the measured signal arises from spin to charge conversion in WTe_2 . According to our measurement geometry and the SHE signal (Fig.2a and 2b), the spin hall angle θ_{SH} is positive based on $I_s \propto s \times I_c$ ³³. This is confirmed by a bias current polarity dependence of the (I)SHE signals (Supplementary Fig. S5). Both the signals R_{SHE} and R_{ISHE} saturate with the magnetization of the injector/detector ferromagnetic Co electrode, as verified from the spin precession Hanle measurements with B_x field in graphene channels (see Supplementary Fig. S7). The observed comparable SHE and ISHE signal magnitudes, their line shapes with magnetic field sweeps are in agreement with the Onsager reciprocity relation³⁴ and demonstrate the generation and detection of pure spin currents in WTe_2 .

To further verify the charge-spin conversion, out-of-plane B_z field sweep measurements were also performed in the ISHE configuration in Dev 3. This Dev 3 consists of monolayer graphene, 11 nm WTe_2 with $1 \mu\text{m}$ width and $25 \Omega \cdot \mu\text{m}^2$ graphene- WTe_2 interface resistance (see Supplementary Table 1 for details about the device). The spin current injected from the FM electrode experience a spin precession in the graphene channel ($L=3.5\mu\text{m}$) as the B_z field is perpendicular to the graphene plane. Subsequently, the spin current gets absorbed $\sim 100\%$ at the graphene/ WTe_2 interface for the monolayer graphene device used here (see Supplementary Fig. S9 d) and give rise to a transversal charge voltage (V_{ISHE}), where $R_{\text{ISHE}}=V_{\text{ISHE}}/I$ (Fig. 2c). Contrary to the in-plane ISHE with B_x field sweep, here the magnetization of FM does not rotate with the B_z field in this field sweep range and remains in-plane. The observed R_{ISHE} is antisymmetric with B_z field. At $B_z=0$, the injected spins are oriented along with the WTe_2 flake without any precession and results in $R_{\text{ISHE}}=0$ as it lacks the right-hand rule for the observation of ISHE^{33,35} in the measured geometry. At a finite B_z field, a maximum (minimum) values of R_{ISHE} are obtained when the precession provides a spin component perpendicular to the WTe_2 long axis. Finally, at a larger B_z field, R_{ISHE} decreases with an increase in

spin precession angle and approach to zero due to complete spin dephasing³⁶. The in-plane (B_x) ISHE measurements in the same Dev 3 is presented in Supplementary Figure S6. Both the in-plane (B_x) and out-of-plane (B_z) measurements unambiguously demonstrate that the in-plane spins are responsible for the induction of the ISHE signal in WTe_2 .

The magnitude of the measured (I)SHE signals (up to ~ 30 m Ω) in WTe_2 are very large, which are two orders of magnitude larger than measured in metals (Pt) in heterostructures with Cu³⁷, and 3 times larger than Pt in heterostructures with graphene^{36,38}, indicating a very large spin Hall angle θ_{SH} in WTe_2 . This can be confirmed by the large spin valve signal reduction since the spin absorption by WTe_2 is the precondition to observe the ISHE^{38,39} (see details in supplementary information Note 1).

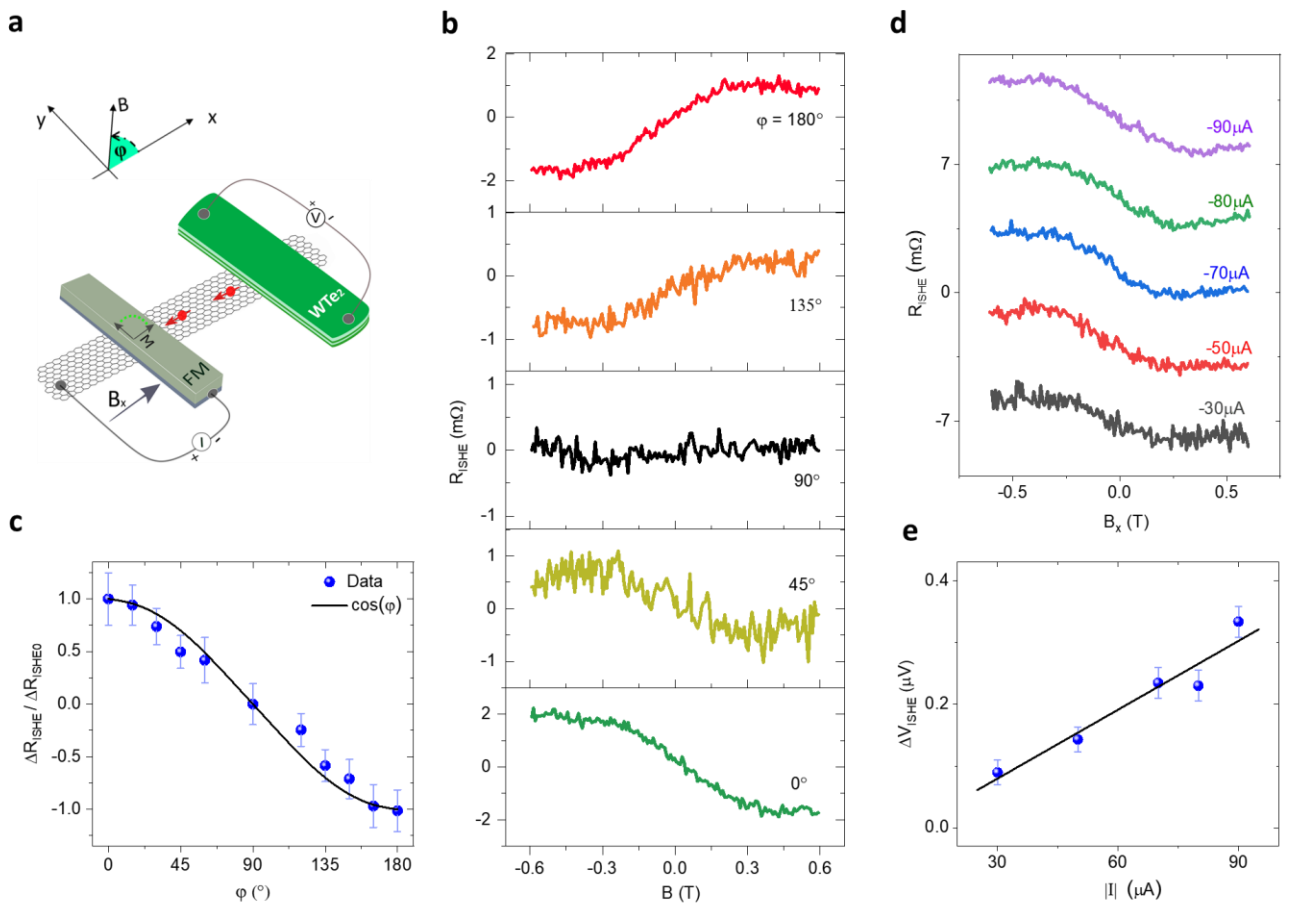


Figure 3. Angle dependence of Inverse spin Hall effect in WTe_2 . **a.** Schematic representation of the ISHE measurement geometry with directions of an applied magnetic field, the detector ferromagnet magnetization, and the spin current. The angle φ is defined as shown in the inset. **b.** The ISHE resistance R_{ISHE} measured at room temperature for various measurement angle orientations for Dev 2 with a graphene channel length of $L_{SHE} = 3.5$ μm . **c.** The normalized magnitude of ΔR_{ISHE} as a function of the magnetic field angle φ . The solid line is the $\cos(\varphi)$ curve. **d,e.** The measured R_{SHE} at different spin injection bias currents with a shift at y-axis for the sake of clarity and the magnitude of the ISHE signal with an applied bias current for the Dev 2. All the measurements were performed at 300K.

The angle-dependent measurements of the ISHE signal³³ were performed in Dev 2 to verify the relation between the direction of the injected spins and the induced charge accumulation in WTe_2 . The measurements were carried out at different in-plane B field along the tilting angle φ respecting to the x-axis (Fig. 3a). As shown in Fig. 3b, the measured R_{ISHE} decreases with the transverse magnetic (x-direction) component and vanishes when the magnetization is aligned with the y-axis. The sign change of R_{ISHE} is observed between $\varphi=0^\circ$ and 180° (π) due to switching of the Co magnetization direction and associated reversal of polarization of the spin current. A null R_{ISHE} signal is observed for $\varphi = 90^\circ$ ($\pi/2$) when the magnetization Co is aligned with the y-axis, as the injected spins are parallel to the WTe_2 long axis and no ISHE voltage is generated in the measured geometry of WTe_2 electrode. The magnitude of the measured ISHE signals ΔR_{ISHE} as a function of the measurement angle φ is shown in Figure 3c. As expected, charge current I_c is proportional to $\mathbf{s} \times \mathbf{I}_s$ (\mathbf{s} is the spin and \mathbf{I}_s is spin current), the angular dependence of the ΔR_{ISHE} is expected to vary with $\cos(\varphi)$. Such angle-dependent behaviors essentially show the characteristics of ISHE signal⁴⁰. Figures 3d and 3e show the ISHE signal measured at different spin injection currents, and as expected ΔV_{ISHE} shows a linear behavior with bias current magnitude. Combining with bias current polarity dependence (Supplementary Fig. S5), we can rule out all the thermal related effects^{41,42}.

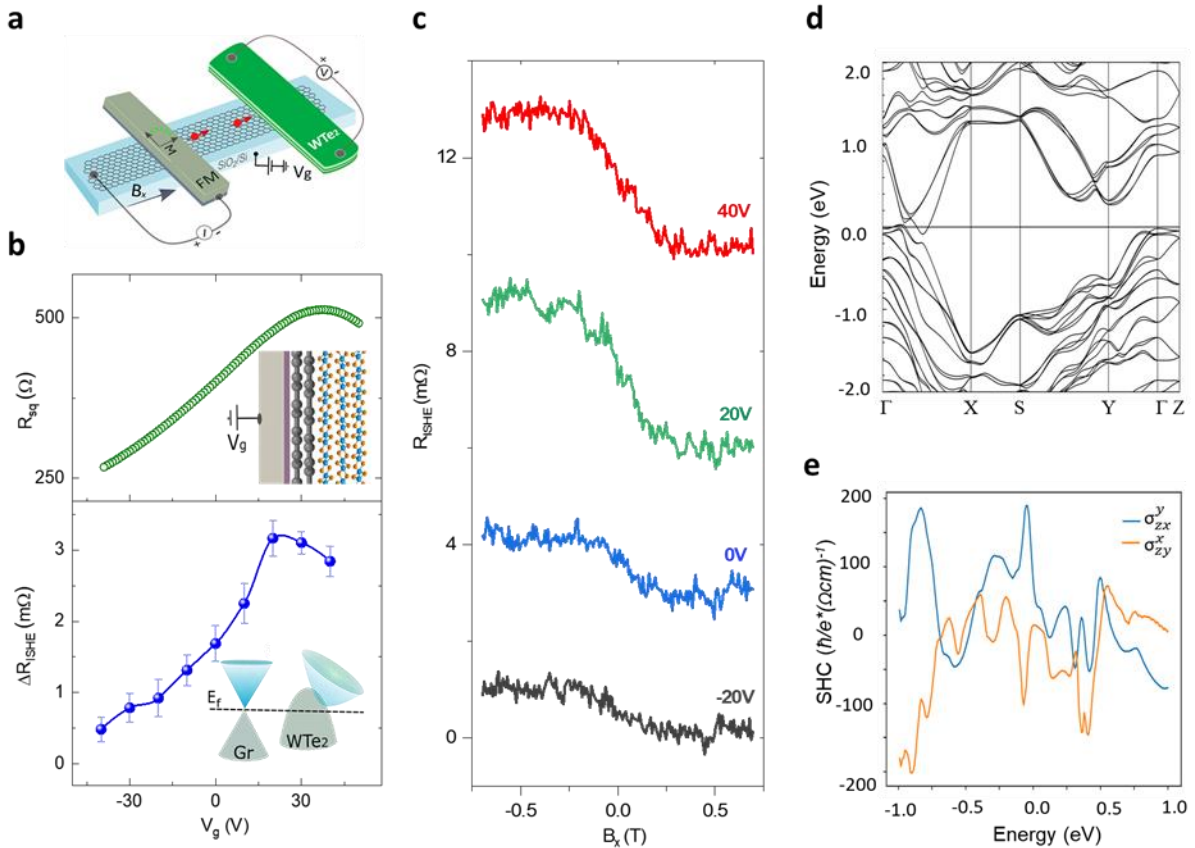


Figure 4. Gate control of the inverse spin Hall signal in the heterostructure. a. The ISHE geometry for the gate voltage dependent measurements. **b.** Top panel: The Dirac curve of the few-layer graphene in the

heterostructure channel measured in a local four-terminal measurement geometry. Bottom panel: Gate dependence of the ΔR_{ISHE} signal magnitude for Dev 2 measured in the range of $V_g = -40$ to 40 V at room temperature. The line is a guide to the eye. The insets are the schematic and band structure of graphene-WTe₂ heterostructure with an applied gate voltage (V_g). **c.** The measured ISHE resistance R_{ISHE} at different gate voltages with a shift at the y-axis for the sake of clarity. **d.** Calculated band structure of bulk WTe₂ in Td phase with the Fermi energy is set to zero. **e.** Calculated SHE conductivity, σ_{zx}^y and σ_{zy}^x , with respect to the Fermi energy position in WTe₂. All the measurements were performed at 300K.

Gate dependence of ISHE measurement was performed in WTe₂-graphene heterostructure (Dev 2) by using the Si/SiO₂ as a back gate (Fig. 4a). The gate voltage dependence of the graphene channel resistance across the heterostructure shows the Dirac point at $V_D = 35$ V (Fig. 4b), while WTe₂ channel resistance does not show much change due to its semi-metallic character (Fig. S3e). The gate dependence of the graphene-WTe₂ interface resistance shows some modulation due to change in the graphene Fermi-energy (Fig. S3d), which may affect the spin absorption efficiency. Figures 4b and 4c show the magnitude of the ISHE signal ΔR_{ISHE} at different gate voltages. Interestingly, we observe a strong increase of the signal magnitude and reaching a maximum as the gate approaches the graphene Dirac point at $V_g = 30$ V. This contrasts with the weak gate dependence of the spin transport signal across the heterostructure (see Supplementary Fig. S8). The gate dependence of spin transport signal (spin valve and Hanle) is known to be strongly dependent on the ferromagnetic tunnel contact resistances⁴³. However, in our case, the nonlocal spin transport signal is almost independent of the gate voltage, while the ISHE signals show a strong modulation. This behavior can be explained by considering the spin detector, i.e. WTe₂-graphene heterostructure instead of the graphene-ferromagnet impedance mismatch⁴³. Part of the enhancement in ΔR_{ISHE} can be due to increased spin absorption by WTe₂, i.e. an increase in effective spin current injected vertically at the graphene-WTe₂ interface when the graphene resistance increase near the Dirac point^{3,4} or (and) the increase of ISHE efficiency with an electric field.

Discussion

The SHE signals observed in our experiment can be rationalized by the conventional bulk SHE and the REE in WTe₂. In an ideal type-I Weyl semimetal (or an ideal topological insulator), in which the bulk Fermi surface vanishes, the bulk SHE is purely contributed by the topological effect⁴⁴. The bulk -induced spin accumulation on the surface is equivalent to that by the Edelstein effect of the topological Fermi arcs, because of the principle of the bulk-boundary correspondence⁴⁵. However, in a type-II Weyl semimetal, the bulk Fermi states always coexists with the Fermi arcs at the Fermi surface. Therefore, we should consider the SHE to include both Fermi surface states and the bulk states effect. Thus, we perform *ab initio* density-functional theory (DFT) calculations^{44,46} (see Methods for details) to evaluate the SHE in WTe₂. The calculated electronic band structure and SHE conductivity for WTe₂ are shown in Figures 4d and 4e. Here, we consider the SHE that can be quantitatively estimated from the spin Berry curvature of the band structure. The SHE refers to the

generation of a spin current $J_j^i = \sigma_{jk}^i E_k$ induced by an electric field E_k , where $i, j, k = x, y, z$ (the crystallographic axes of WTe_2), and J_j^i represents a spin current along the j direction with a spin polarization along i . The SHE conductivity σ_{jk}^i characterizes the strength of the SHE. For a charge current along the ab plane and spin current along the c axis, we obtain the corresponding in-plane SHE conductivities in the range of $\sigma_{SH} = 14 - 96 (\hbar/e)(\Omega \cdot cm)^{-1}$ due to the large crystal anisotropy. Taking the electronic conductivity of WTe_2 from our measurement, we estimate the theoretical maximum SHE to be with a spin Hall angle of $\theta_{SH} = \frac{\sigma_{SH}}{\sigma_{xx}} = 17\%$. The calculated large θ_{SHE} can qualitatively account for the observation of the large SHE signals in our experiments. This is also confirmed by a recent theory paper⁴⁷, which suggests a large spin Hall angle in WTe_2 . Furthermore, as shown in Fig. 4e, the calculated SHE conductivity is also found to be very sensitive and depends on the position of the Fermi energy in WTe_2 . The calculated σ_{SHE} can be considerably tuned by a small change in energy, such as a tiny change in energy at 100 meV below the Fermi energy can cause a change of σ_{SHE} by nearly an order of magnitude. However, experimentally we could not tune the surface states of WTe_2 to the Fermi level by the application of gate voltage^{21,24}.

To be noted, one cannot extract spin Hall angle θ_{SH} and spin diffusion length λ_{WTe_2} at the same time by fitting the out-of-plane (I)SHE signal³⁶ or solving the in-plane case equation³⁸ due to the entanglement of the two parameters. Therefore, we take $\theta_{SH} = 0.013$ from the literature with comparable WTe_2 thickness²⁷. Consequently, the data fitting results in a spin diffusion length of $\lambda_{WTe_2} = 8 \pm 0.9$ nm. To verify the result, a numerical solution to the in-plane ISHE signal was also obtained. Substituting λ_{WTe_2} into the plot of $\theta_{SH} \sim \lambda_{WTe_2}$, we find the $\theta_{SH} = 0.014$, which is consistent with the literature (see details in Supplementary Note 2). For estimation of these spin parameters, we used the Dev 3 with monolayer graphene and a narrow and thin WTe_2 flake (\sim width = 1 μ m and thickness = 11 nm) having a very low WTe_2 -graphene interface resistance $\sim 25 \Omega \cdot \mu m^2$, which is suitable for the use of the 1D model calculation (shown in Table 1). In contrast, for thicker WTe_2 flakes, the WTe_2 -graphene interface resistance is usually hundreds of Ohms due to their poor van der Waals adhesion. Therefore, an experimental quantification of the SHE parameters in WTe_2 by the conventional spin absorption method^{38,39} is not possible for Dev 1 and 2. Nevertheless, the calculations suggest that the spin Hall angle θ_{SH} is larger for the thicker WTe_2 . This implies a possible presence of a thickness-dependent spin Hall angle and the dominance of SHE in our measurements. More detailed thickness-dependent studies are needed to investigate these effects and disentanglement of the contributions of the SHE and REE in the observed signal^{5,48}.

Conclusion and Outlook

The emergent Weyl semimetal WTe_2 is shown here to be a promising material for charge-spin conversion at room temperature due to its unique electronic band structure giving rise to huge spin-orbit coupling and spin-polarized bulk and surface states. Particularly, the strong spin Hall

signal in the WTe₂-graphene hybrid devices and the gate tunability of the spin absorption process provide a new tool for potential application in future spintronic device architectures. Furthermore, as predicted in theoretical calculations, the spin Hall conductivity can be controlled by using Weyl semimetals with tunable Fermi-level¹⁰ and alloys with tunable-resistivity^{37,49}. This will allow achieving systematic control over the charge-spin conversion via electrical and optical means and a better understanding of the Weyl physics. Such measures providing large charge-spin conversion efficiency in Weyl semimetals at room temperature can be used to switch or oscillate the magnetization of nanomagnets with a very low current density. These developments will have a huge potential for emergent spin-orbit induced phenomena and applications in ultralow power magnetic random-access memory and spin logic circuits^{29,50}.

Methods

Device Fabrication - The exfoliated few layers graphene was mechanically exfoliated onto the n-doped Si substrate with 300 nm SiO₂. The CVD graphene was transferred on the substrate Si/SiO₂ substrate by wet transfer method and followed by EBL and Ar patterning. The WTe₂ flakes were exfoliated on PDMS and dry-transferred on to the graphene flake under a microscope using a home-built micromanipulator transfer stage. The CVD graphene-WTe₂ devices were made by exfoliation of WTe₂ and dry transfer process inside the glove box. Contacts to graphene and WTe₂ were defined by standard electron beam lithography and lift-off process. For the preparation of ferromagnetic tunnel contacts to graphene, a two-step deposition of 0.3 nm of Ti and oxidation process was carried out, followed by a 100 nm of Co deposition. The ferromagnetic tunnel contact (TiO₂/Co) resistances on graphene channel were in the range of few kΩs.

Measurements - The measurements are performed in a vacuum system equipped with a variable angular rotation facility and with an electromagnet with a magnetic field up to 0.8 Tesla. The electronics used for the measurements are Keithley 6221 current source, Keithley 2182A nanovoltmeter and Keithley 2612B source meter for application of gate voltages.

Theoretical calculation methods - We perform ab initio density-functional theory (DFT) calculations and then project the DFT wave functions to atomic-like Wannier functions with the FPLO program⁴⁶. Based on highly symmetric Wannier functions, we construct a tight-binding-type Hamiltonian that can fully reproduce the DFT results. Using the material-specific effective Hamiltonian, we employed the Kubo formula approach⁴⁴ to calculate the SHE conductivity.

Data availability

The data that support the findings of this study are available from the corresponding authors on reasonable request.

Acknowledgments

The authors at Chalmers University of Technology, Sweden acknowledge financial supports from EU FlagEra project (from Swedish Research Council VR No. 2015-06813), Swedish Research Council VR project grants (No. 2016-03658), EU Graphene Flagship (No. 604391), Graphene center and the AoA Nano program at Chalmers University of Technology. The authors from University of Science and Technology Beijing, Beijing, China, acknowledge financial supports from the National Basic Research Program of China (Grant No. 2015CB921502) and the National Natural Science Foundation of China (Grant Nos. 51731003, 51471029). Bing Zhao would like to thank the financial support from the program of China Scholarships Council (File No.

201706460036) to visit Chalmers. We thank our colleagues at the Quantum Device Physics Laboratory and Nanofabrication Laboratory at Chalmers University of Technology for their support.

Author information

Affiliations

¹Beijing Advanced Innovation Center for Materials Genome Engineering, School of Materials Science and Engineering, University of Science and Technology Beijing, Beijing 100083, China

²Department of Microtechnology and Nanoscience, Chalmers University of Technology, SE-41296, Göteborg, Sweden

³Max Planck Institute for Chemical Physics of Solids, 01187 Dresden, Germany

⁴Department of Condensed Matter Physics, Weizmann Institute of Science, Rehovot 7610001, Israel

⁵Graphene Center, Chalmers University of Technology, SE-41296 Göteborg, Sweden.

Contributions

SPD and BZ conceived the idea and designed the experiments. BZ, DK, BK, and SPD fabricated and measured the devices at Chalmers University of Technology. BZ and SPD analyzed, interpreted the experimental data, compiled the figures and wrote the manuscript. DK, BK, AHM, BY, XX, YJ discussed the results and provided feedback on the manuscript. Y.Z., H.F. and B.Y. performed theoretical calculations on the band structure and SHE conductivity. SPD, YJ, BY supervised the experimental and theoretical research. SPD supervised the project.

Competing interests

The authors declare no competing financial interests.

Corresponding authors:

Correspondence and requests for materials should be addressed to Saroj P. Dash, Email: saroj.dash@chalmers.se

References

1. Novoselov, K. S., Mishchenko, A., Carvalho, A. & Castro Neto, A. H. 2D materials and van der Waals heterostructures. *Science* (80-.). **353**, aac9439 (2016).
2. Manzeli, S., Ovchinnikov, D., Pasquier, D., Yazyev, O. V. & Kis, A. 2D transition metal dichalcogenides. *Nat. Rev. Mater.* **2**, 17033 (2017).
3. Dankert, A. & Dash, S. P. Electrical gate control of spin current in van der Waals heterostructures at room temperature. *Nat. Commun.* **8**, 16093 (2017).
4. Yan, W. *et al.* A two-dimensional spin field-effect switch. *Nat. Commun.* **7**, 13372 (2016).
5. Safeer, C. K. *et al.* Room-Temperature Spin Hall Effect in Graphene/MoS₂ van der Waals Heterostructures. *Nano Lett.* **19**, 1074–1082 (2019).
6. Offidani, M., Milletari, M., Raimondi, R. & Ferreira, A. Optimal Charge-to-Spin Conversion in Graphene on Transition-Metal Dichalcogenides. *Phys. Rev. Lett.* **119**, 196801 (2017).
7. Wang, Q. H., Kalantar-Zadeh, K., Kis, A., Coleman, J. N. & Strano, M. S. Electronics and optoelectronics of two-dimensional transition metal dichalcogenides. *Nat. Nanotechnol.* **7**, 699–712 (2012).
8. Burkov, A. Topological semimetals. *Nat. Mater.* **15**, 1145–1148 (2016).

9. Wu, S. *et al.* Observation of the quantum spin Hall effect up to 100 kelvin in a monolayer crystal. *Science* (80-.). **359**, 76–79 (2018).
10. Armitage, N. P., Mele, E. J. & Vishwanath, A. Weyl and Dirac semimetals in three-dimensional solids. *Rev. Mod. Phys.* **90**, 15001 (2018).
11. Zheng, H. & Zahid Hasan, M. Quasiparticle interference on type-I and type-II Weyl semimetal surfaces: a review. *Adv. Phys. X* **3**, 1466661 (2018).
12. Yan, B. & Felser, C. Topological Materials: Weyl Semimetals. *Annu. Rev. Condens. Matter Phys.* **8**, 337–354 (2017).
13. Ali, M. N. *et al.* Large, non-saturating magnetoresistance in WTe₂. *Nature* **514**, 205–208 (2014).
14. Shekhar, C. *et al.* Extremely large magnetoresistance and ultrahigh mobility in the topological Weyl semimetal candidate NbP. *Nat. Phys.* **11**, 645–649 (2015).
15. Xiong, J. *et al.* Evidence for the chiral anomaly in the Dirac semimetal Na₃Bi. **350**, 1314–1317 (2015).
16. Zhang, Y., van den Brink, J., Felser, C. & Yan, B. Electrically tuneable nonlinear anomalous Hall effect in two-dimensional transition-metal dichalcogenides WTe₂ and MoTe₂. *2D Mater.* **5**, 044001 (2018).
17. Lv, B. Q. *et al.* Observation of Fermi-Arc Spin Texture in TaAs. *Phys. Rev. Lett.* **115**, 217601 (2015).
18. Johansson, A., Henk, J. & Mertig, I. Edelstein effect in Weyl semimetals. *Phys. Rev. B* **97**, 085417 (2018).
19. Sun, Y., Wu, S.-C. & Yan, B. Topological surface states and Fermi arcs of the noncentrosymmetric Weyl semimetals TaAs, TaP, NbAs, and NbP. *Phys. Rev. B* **92**, 115428 (2015).
20. Berger, A. N. *et al.* Temperature-driven topological transition in 1T'-MoTe₂. *npj Quantum Mater.* **3**, 2 (2018).
21. Bruno, F. Y. *et al.* Observation of Large Topologically Trivial Fermi-Arcs in the Candidate Type-II Weyl Semimetal WTe₂. *Phys. Rev. B* **94**, 121112 (2016).
22. Li, P. *et al.* Evidence for topological type-II Weyl semimetal WTe₂. *Nat. Commun.* **8**, 2150 (2017).
23. Wu, Y. *et al.* Observation of Fermi arcs in the type-II Weyl semimetal candidate WTe₂. *Phys. Rev. B* **94**, 121113 (2016).
24. Wang, C. *et al.* Observation of Fermi arc and its connection with bulk states in the candidate type-II Weyl semimetal WTe₂. *Phys. Rev. B* **94**, 241119 (2016).
25. Jiang, J. *et al.* Signature of Strong Spin-Orbital Coupling in the Large Nonsaturating Magnetoresistance Material WTe₂. *Phys. Rev. Lett.* **115**, 166601 (2015).
26. Wang, Q. *et al.* Room-Temperature Nanoseconds Spin Relaxation in WTe₂ and MoTe₂ Thin Films. *Adv. Sci.* **5**, 1700912 (2018).
27. MacNeill, D. *et al.* Control of spin-orbit torques through crystal symmetry in WTe₂/ferromagnet bilayers. *Nat. Phys.* **13**, 300–305 (2017).
28. Li, P. *et al.* Spin-momentum locking and spin-orbit torques in magnetic nano-heterojunctions composed of Weyl semimetal WTe₂. *Nat. Commun.* **9**, 3990 (2018).
29. Garelo, K., F. Y. *et al.* SOT-MRAM 300nm integration for low power and ultrafast embedded memories. *arXiv Prepr. arXiv1810.10356* (2018).
30. Feng, B. *et al.* Spin texture in type-II Weyl semimetal WTe₂. *Phys. Rev. B* **94**, 195134 (2016).
31. Sinova, J., Valenzuela, S. O., Wunderlich, J., Back, C. H. & Jungwirth, T. Spin Hall effects. *Rev. Mod. Phys.* **87**, 1213–1260 (2015).
32. Ando, K. & Saitoh, E. Observation of the inverse spin Hall effect in silicon. *Nat. Commun.* **3**, 626–629 (2012).
33. Kimura, T., Otani, Y., Sato, T., Takahashi, S. & Maekawa, S. Room-Temperature Reversible Spin Hall Effect. *Phys. Rev. Lett.* **98**, 156601 (2007).
34. Onsager, L. Reciprocal Relations in Irreversible Processes. I. *Phys. Rev.* **37**, 405–426 (1931).
35. Valenzuela, S. O. & Tinkham, M. Direct electronic measurement of the spin Hall effect. *Nature* **442**, 176–179 (2006).
36. Savero Torres, W. *et al.* Spin precession and spin Hall effect in monolayer graphene/Pt nanostructures. *2D Mater.*

- 4, 041008 (2017).
37. Sagasta, E. *et al.* Tuning the spin Hall effect of Pt from the moderately dirty to the superclean regime. *Phys. Rev. B* **94**, 060412 (2016).
 38. Yan, W. *et al.* Large room temperature spin-to-charge conversion signals in a few-layer graphene/Pt lateral heterostructure. *Nat. Commun.* **8**, 661 (2017).
 39. Niimi, Y. *et al.* Extrinsic Spin Hall Effect Induced by Iridium Impurities in Copper. *Phys. Rev. Lett.* **106**, 126601 (2011).
 40. Fujiwara, K. *et al.* 5d iridium oxide as a material for spin-current detection. *Nat. Commun.* **4**, 2893 (2013).
 41. Slachter, A., Bakker, F. L., Adam, J.-P. & van Wees, B. J. Thermally driven spin injection from a ferromagnet into a non-magnetic metal. *Nat. Phys.* **6**, 879–882 (2010).
 42. Sierra, J. F. *et al.* Thermoelectric spin voltage in graphene. *Nat. Nanotechnol.* **13**, 107–111 (2018).
 43. Han, W. *et al.* Tunneling Spin Injection into Single Layer Graphene. *Phys. Rev. Lett.* **105**, 167202 (2010).
 44. Sun, Y., Zhang, Y., Felser, C. & Yan, B. Strong Intrinsic Spin Hall Effect in the TaAs Family of Weyl Semimetals. *Phys. Rev. Lett.* **117**, 146403 (2016).
 45. Essin, A. M. & Gurarie, V. Bulk-boundary correspondence of topological insulators from their respective Green's functions. *Phys. Rev. B* **84**, 125132 (2011).
 46. Eschrig, H. Full-potential nonorthogonal local-orbital minimum-basis band-structure scheme. *Phys. Rev. B - Condens. Matter Mater. Phys.* **59**, 1743–1757 (1999).
 47. Zhou, J., Qiao, J., Bournel, A. & Zhao, W. Intrinsic spin Hall conductivity of the semimetals MoTe₂ and WTe₂. *Phys. Rev. B* **99**, 060408 (2019).
 48. Ghiasi, T. S., Kaverzin, A. A., Blah, P. J. & van Wees, B. J. Charge-to-Spin Conversion by the Rashba-Edelstein Effect in 2D van der Waals Heterostructures up to Room Temperature. arXiv preprint arXiv:1905.01371. (2019). doi:arXiv preprint arXiv:1905.01371.
 49. Chang, T.-R. *et al.* Prediction of an arc-tunable Weyl Fermion metallic state in MoxW_{1-x}Te₂. *Nat. Commun.* **7**, 10639 (2016).
 50. Soumyanarayanan, A., Reyren, N., Fert, A. & Panagopoulos, C. Emergent phenomena induced by spin-orbit coupling at surfaces and interfaces. *Nature* **539**, 509–517 (2016).

Supplementary Information

Observation of Spin Hall Effect in Weyl Semimetal WTe_2 at Room Temperature

Bing Zhao^{1,2}, Dmitrii Khokhriakov², Yang Zhang³, Huixia Fu⁴, Bogdan Karpiak², Anamul Md. Hoque², Xiaoguang Xu¹, Yong Jiang¹, Binghai Yan⁴, Saroj P. Dash^{2,5*}

¹Beijing Advanced Innovation Center for Materials Genome Engineering, School of Materials Science and Engineering, University of Science and Technology Beijing, Beijing 100083, China

²Department of Microtechnology and Nanoscience, Chalmers University of Technology, SE-41296, Göteborg, Sweden

³Max Planck Institute for Chemical Physics of Solids, 01187 Dresden, Germany

⁴Department of Condensed Matter Physics, Weizmann Institute of Science, Rehovot 7610001, Israel

⁵Graphene Center, Chalmers University of Technology, SE-41296 Göteborg, Sweden.

Corresponding author: *Saroj P. Dash, Email: saroj.dash@chalmers.se

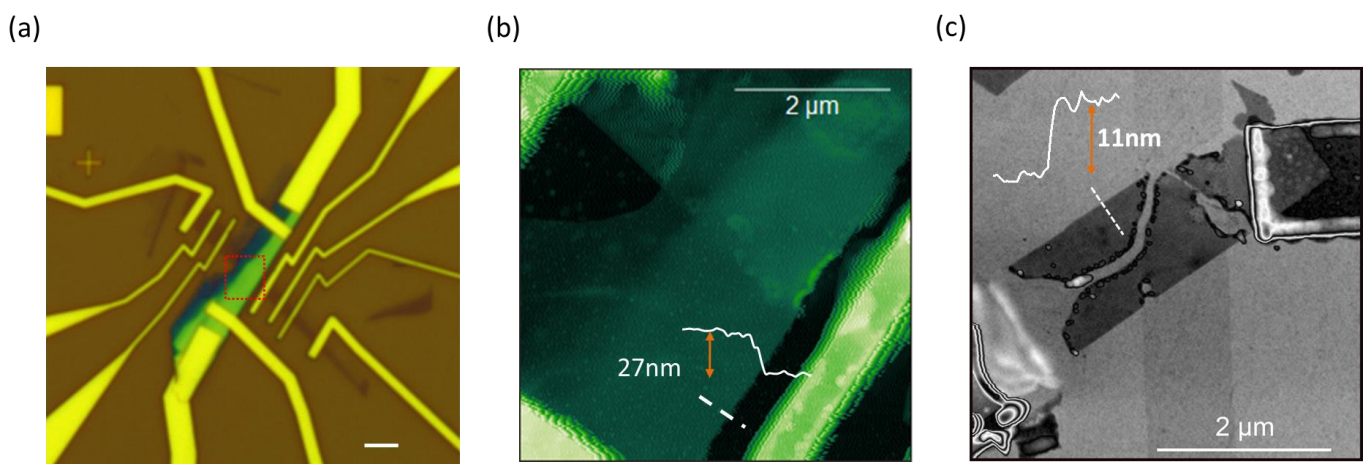


Figure S1. Devices with WTe_2 -graphene heterostructure. (a) Optical micrograph of Device 1, with WTe_2 -graphene heterostructure and ferromagnetic (TiO_2 1 nm/ Co 60 nm) contacts on graphene for detection and creation of (I)SHE in WTe_2 . The scale bar is 2 μm . (b) Atomic force microscope (AFM) picture of the heterostructure area (red mark in (a)). The inset is the thickness profile of WTe_2 on few-layer graphene along the white dash line showing the WTe_2 thickness is 27 nm in Device 1. (c) AFM picture and thickness profile of Dev 3 (after the device burnout) showing WTe_2 thickness to be 11 nm on monolayer CVD graphene.

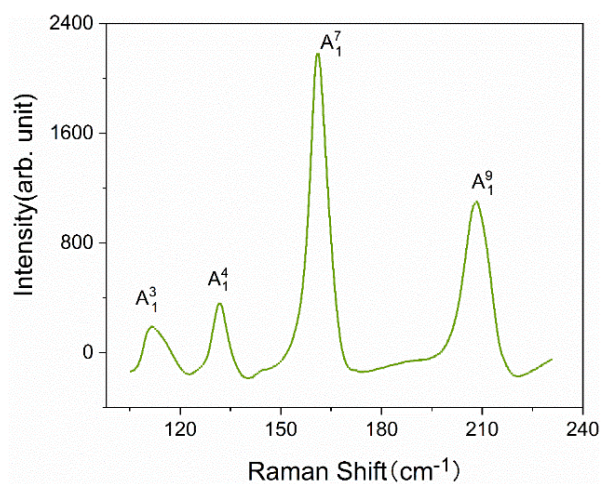


Figure S2. Raman characterization of WTe₂. The Raman spectrum of bulk WTe₂ along *c*- axis using a LASER with a 638 nm wavelength. The characteristic peaks¹ located at about 112, 132, 161, and 208 cm⁻¹ corresponding to the A₁³, A₁⁴, A₁⁷ and A₁⁹, showing the T_d-phase nature of WTe₂.

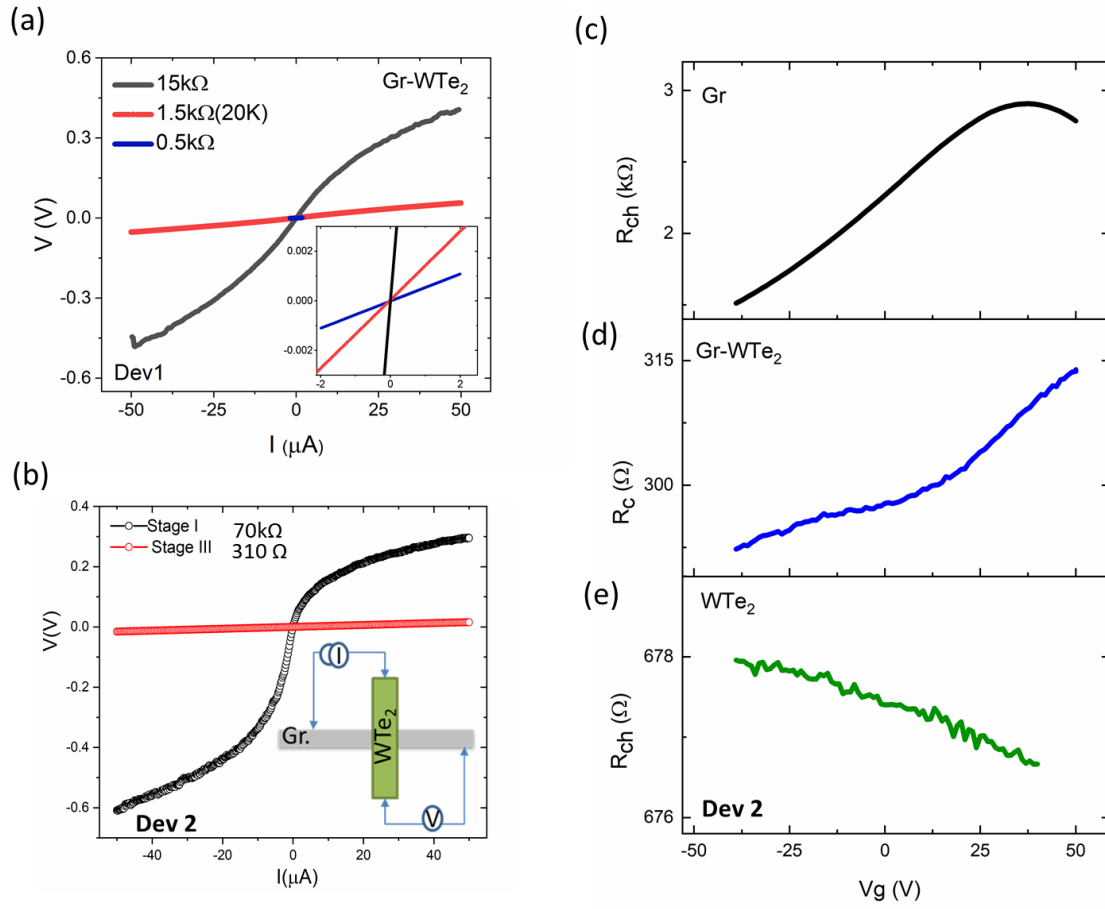


Figure S3. Electrical characterization of the graphene-WTe₂ heterostructure in Dev 1 and Dev 2. (a) The current-voltage (IV) characteristics of the graphene-WTe₂ interface resistance of Dev 1 at different stages measured in a four-terminal geometry. The inset is a zoom-in part around zero bias. The interface resistance of graphene-WTe₂ is about 15 kΩ at stage II, which is reduced to 500 Ω at stage III. **(b)** Current-voltage (IV) curve of the WTe₂-graphene interface contact at different stages of resistances, stage I = 70 kΩ and stage III = 310 Ω at room temperature. The inset shows the schematic of the four-terminal geometry used for the IV measurements. Ultimately, all the devices stabilized at a low contact resistance of 300-500 Ω, which is suitable for (I)SHE measurements. **(c-e)** Gate dependence of graphene (Gr) channel resistance, WTe₂-graphene contact resistance and WTe₂ channel resistance in Dev 2, respectively.

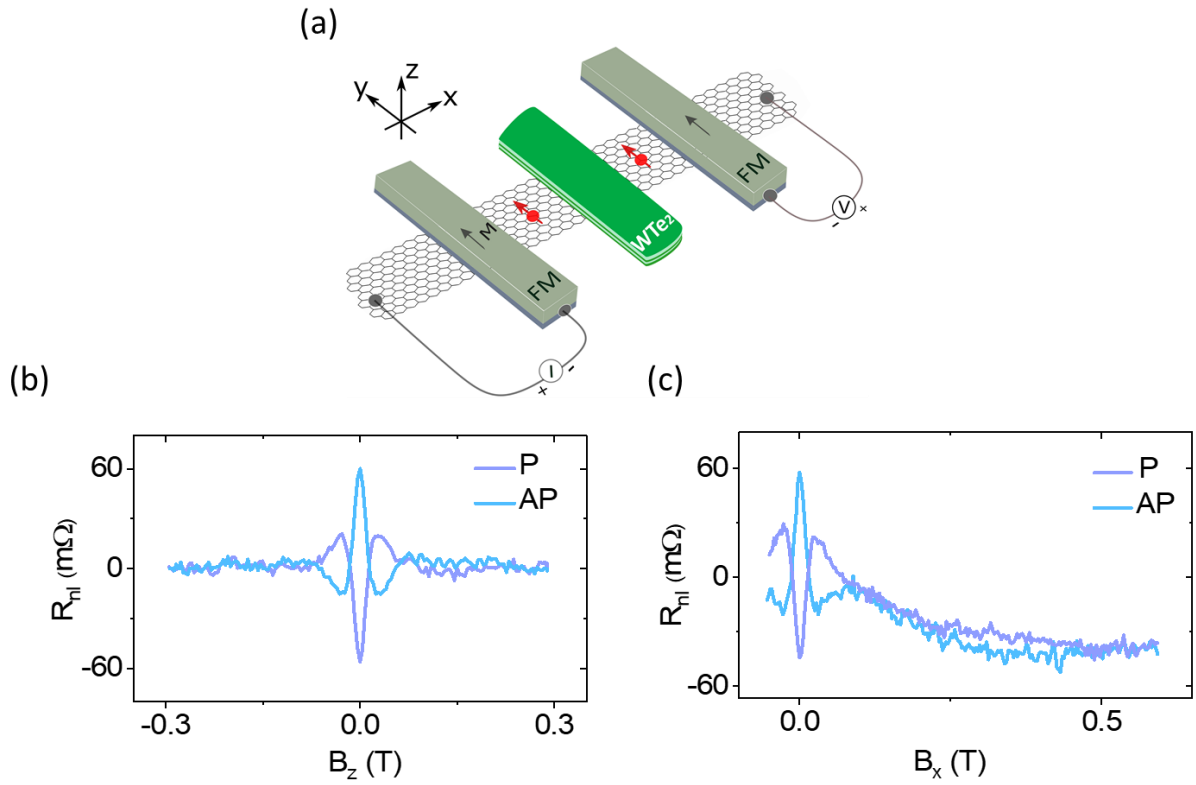


Figure S4. Spin transport and precession across the graphene- WTe_2 heterostructure before the spin absorption in Dev 2. (a) Schematic of the non-local Hanle measurement geometry in the WTe_2 -graphene heterostructure device. (b, c) Hanle spin precession signal for different magnetic field sweep directions B_z and B_x for both the parallel (P) and anti-parallel (AP) alignment of ferromagnetic Co electrodes in Dev 2 at room temperature in stage1 (before the spin absorption). A linear background is removed from the measured spin signals.

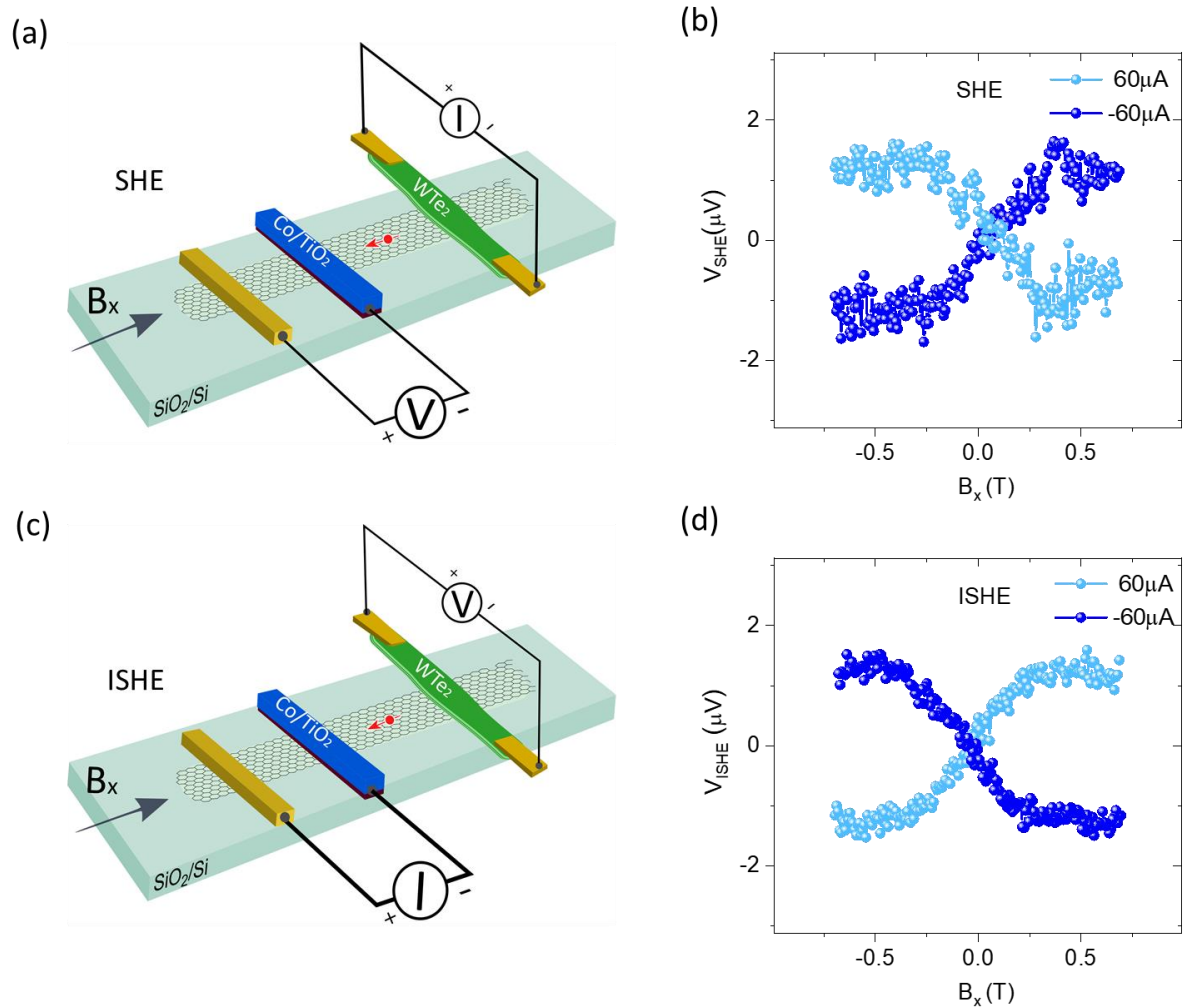


Figure S5. Charge-to-spin conversion (SHE) and inverse charge-to-spin conversion (ISHE) effect in graphene-WTe₂ heterostructures with different bias polarity for Dev 1. (a, b) SHE measurement geometry and data with an applied bias current of +60μA and -60μA along with the WTe₂ flake. The spin current induced at the WTe₂-graphene interface diffuse towards the Co/TiO₂ detector contact. (c, d) ISHE measurement geometry and the measured signal, where the spin current is injected from the Co/TiO₂ contact with +60μA and -60μA bias currents. The injected spin current diffuse towards the WTe₂-graphene heterostructure and produce the ISHE signal. For the sake of clarity, the linear background is subtracted from the (I)SHE signals.

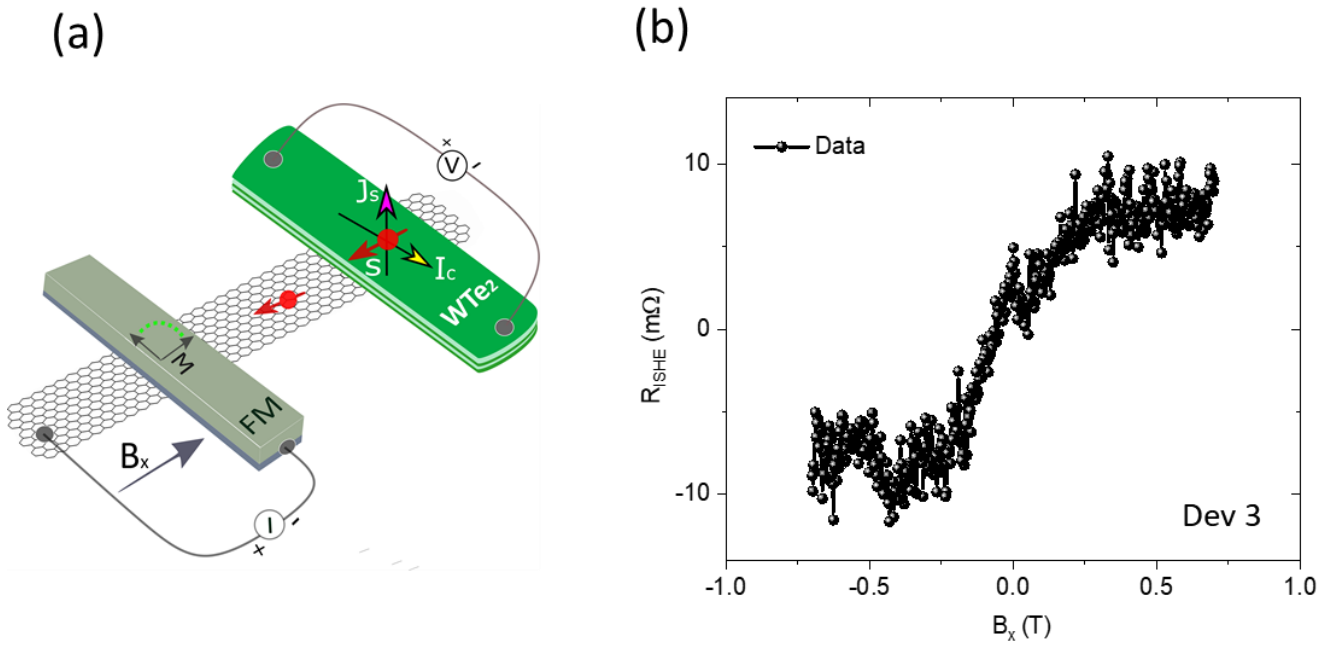


Figure S6. Inverse spin Hall effect (ISHE) in monolayer graphene-WTe₂ heterostructure in Dev 3. (a, b) ISHE measurement geometry and measured signal with sweep of magnetic field B_x in Dev 3 with spin injection bias current of $100\mu\text{A}$ and $V_g = -60\text{V}$, at room temperature. The Dev 3 consists of monolayer CVD graphene and a narrow and thin WTe₂ flake (\sim width = $1\mu\text{m}$ and thickness = 11nm) heterostructure with interface resistance $25\Omega\mu\text{m}^2$. A linear background is subtracted from the signal.

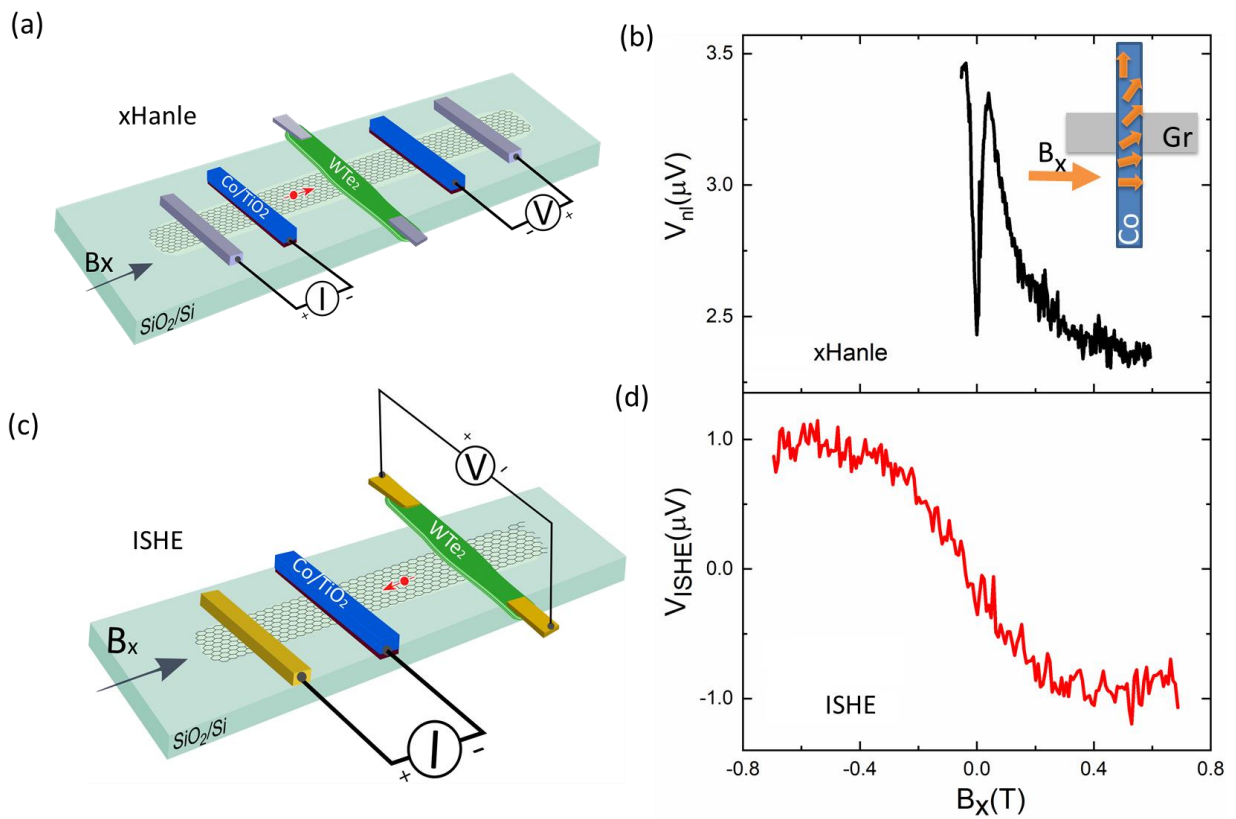


Figure S7. Estimation of magnetization saturation field from Hanle measurements. (a, b) Hanle spin precession measurement geometry and data for the graphene-WTe₂ heterostructure channel with magnetic field sweep in the direction of B_x at room temperature for Dev2 at stage-I. Inset in (b) is the schematic for the rotation of the Co magnetization when sweeping a B field in the x-direction. (c, d) Inverse SHE measurement geometry and data with the use of same Co as spin injector contact in Dev 2. Both measurements were applied with $-60\mu\text{A}$.

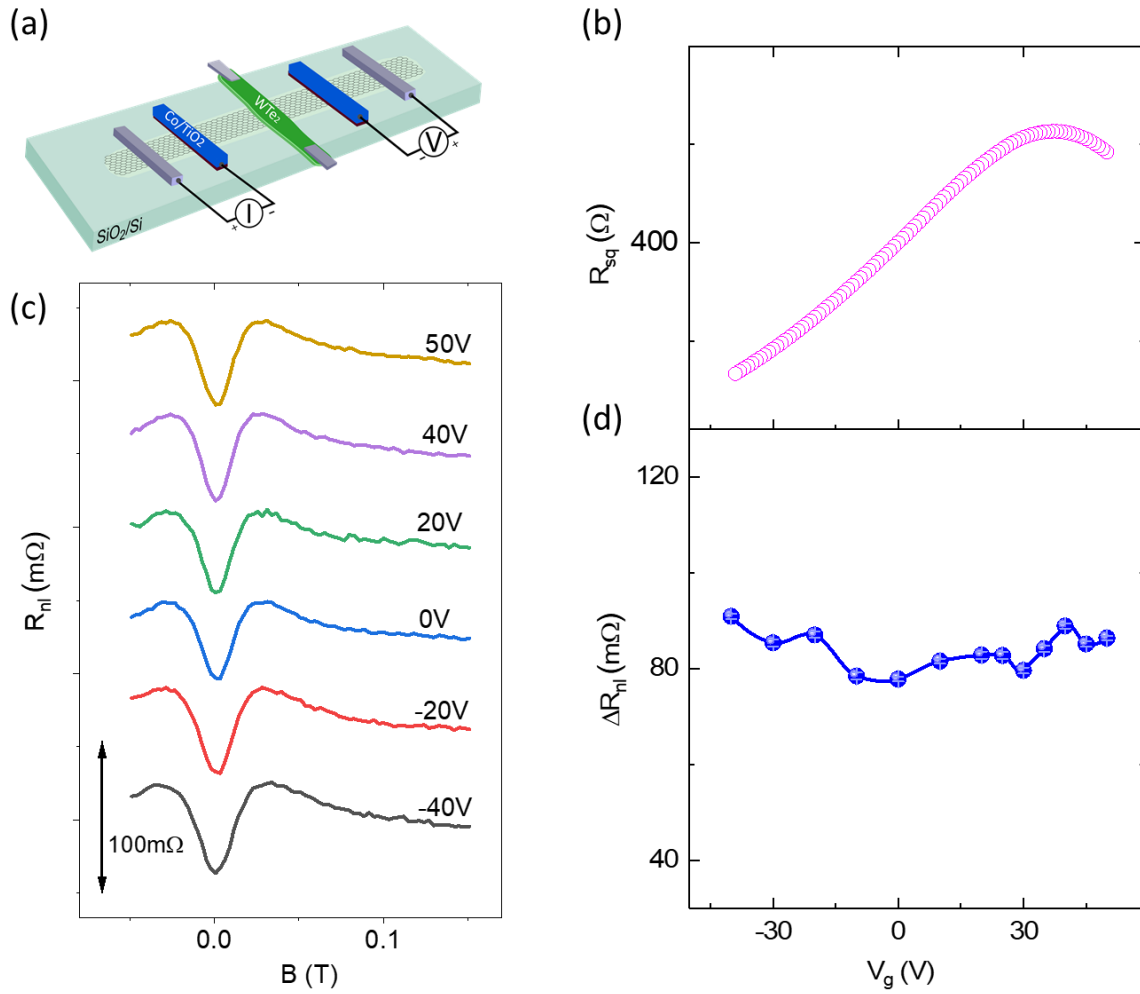


Figure S8. Gate dependence of nonlocal spin signal across the graphene-WTe₂ heterostructure of Dev 2 in stage-I, before spin absorption. (a) Schematics of the nonlocal spin transport measurement geometry. (b, c, d) Gate dependence of the graphene channel square resistance, Hanle spin precession signal, and the magnitude of the spin signal across the WTe₂-Gr heterostructure at stage I (before spin absorption) in Dev 2 at room temperature, respectively. The error bars are within the data points.

Note 1. Spin absorption effect at the WTe₂-graphene interface

The spin current in the graphene channel can be absorbed by WTe₂ due to its high SOC², highly depending on the contact resistance of the graphene-WTe₂ interface^{3,4}. We observed that the van der Waals interface contact resistance of graphene-WTe₂ usually evolved during the measurements (Fig. S3a and S3b) in the exfoliated few-layer graphene and 20-30 nm WTe₂ devices (Dev 1 and Dev 2). Three distinctly different resistance states of the graphene-WTe₂ interface were observed at room temperature. As shown in Fig. S3b, stage-I shows a tunneling type conduction, with zero-bias contact resistance (ZCR) of about 70 k Ω . Stage-II is an intermediate state with ZCR around 3k Ω (not shown in the figure). Ultimately the stage-III show a lower interface with a very stable ZCR of 310 Ω . Similar behaviors are observed in both Dev 1 and Dev 2. Due to the decrease of the resistance and the ultimate formation of low stable interface resistance between graphene and WTe₂, the oxidation of WTe₂ at the interface can be ruled out. Such a contact behaviour is believed to be caused by a gap or air bubble at the interface introduced in the WTe₂ flake dry transfer process. During the fabrication, the use of a vacuum treatment of the heterostructure before spin coating with e-beam resist, resulted in a faster evolution of the interface resistance. Moreover, the graphene channel covered by WTe₂ is found to be very stable with an almost unchanged Dirac Point and other parameters (see Table 1), which shows a harmonious van der Waals bonding nature of graphene and WTe₂. With the evolution of graphene-WTe₂ interface resistance, the spin current in the graphene channel gets increasingly absorbed by the WTe₂ at the interface. Direct evidence for this is the obvious decrease of the spin valve signal by 81.3% from 106 m Ω to 20 m Ω as the contact resistance changes from stage I=70 k Ω to stage III= 310 Ω (Fig. S9c). Similar behavior is also observed in Dev 1 (about a 50% decrease, see Fig. S9b). Moreover, the TiO₂/Co contact resistances and graphene channel resistance at stage-I and -III remain comparable. Therefore, we can conclude that the strong spin absorption effect is the origin for the reduction of the spin valve signal from the state I to stage III^{3,4}, which allowed us to measure the ISHE signals in our devices. As expected, no (I)SHE signals could be measured for higher graphene-WTe₂ contact resistances in stage I, because of very-low spin absorption at the interface.

However, in the Dev 3, the heterostructure of CVD monolayer graphene and 11 nm WTe₂ devices, a much lower interface resistance 25 $\Omega\mu\text{m}^2$ is obtained (see Table 1 for Dev 3), which guarantees the transparent interface between WTe₂ and graphene. In this device, no spin valve signal could be observed across the heterostructure channel (Fig. S9d), which suggests about 100% spin absorption at the WTe₂-graphene interface. To verify the spin injection and detection of the ferromagnetic contacts of Co/TiO₂ in the Dev 3, the spin valve and Hanle measurement of the only area graphene channel outside the WTe₂ were also performed. The standard spin valve and Hanle signal can be observed. Furthermore, the use of a narrow WTe₂ (1 μm), less than spin diffusion length in graphene, makes sure that the 1D model can be used in the analysis.

Table 1

Parameters of the devices. $L_{ch,Gr}$, w_{Gr} , $R_{sq,Gr}$, D_s , τ_s , λ_{Gr} , are the channel length, width, square resistance, spin diffusion constant, spin lifetime and spin diffusion length of graphene, respectively. t_{WTe_2} , w_{WTe_2} , ρ_{WTe_2} are the thickness, width, resistivity of WTe_2 , respectively. L_{SH} is the channel length of (I)SHE measurement. R_{c,WTe_2-Gr} is the contact resistance of the WTe_2 -Gr heterostructure. R_cA is the product of the heterostructure contact resistance and area. Dev 1 and Dev 2 uses few layers of exfoliated graphene, where as Dev 3 is made up of monolayer CVD graphene.

		$L_{ch,Gr}$ (μm)	D_s (m^2/s)	τ_s (ps)	λ_{Gr} (μm)	R_{c,WTe_2-Gr} ($k\Omega$)	w_{Gr} (μm)	L_{SH} (μm)	t_{WTe_2} (nm)	w_{WTe_2} (μm)	R_cA ($k\Omega\mu m^2$)	$R_{sq,Gr}$ ($k\Omega$)	ρ_{WTe_2} ($\mu\Omega m$)
Dev 1	stage I	5.1	0.0141	316	2.11	50	1.35	2.6	27	3	203	0.423	8.9
	stage III		0.0188	202	1.95	0.5					2.03		
Dev 2	stage I	6.9	0.0154	326	2.24	70	1.3	3.5	20	5	440	0.496	8.9
	stage III		0.0178	299	2.31	0.31					1.95		
Dev 3	$V_g = -60V$	6.9	0.03011	185	2.4	0.025	1	3.5	11	1	0.025	0.546	9.04

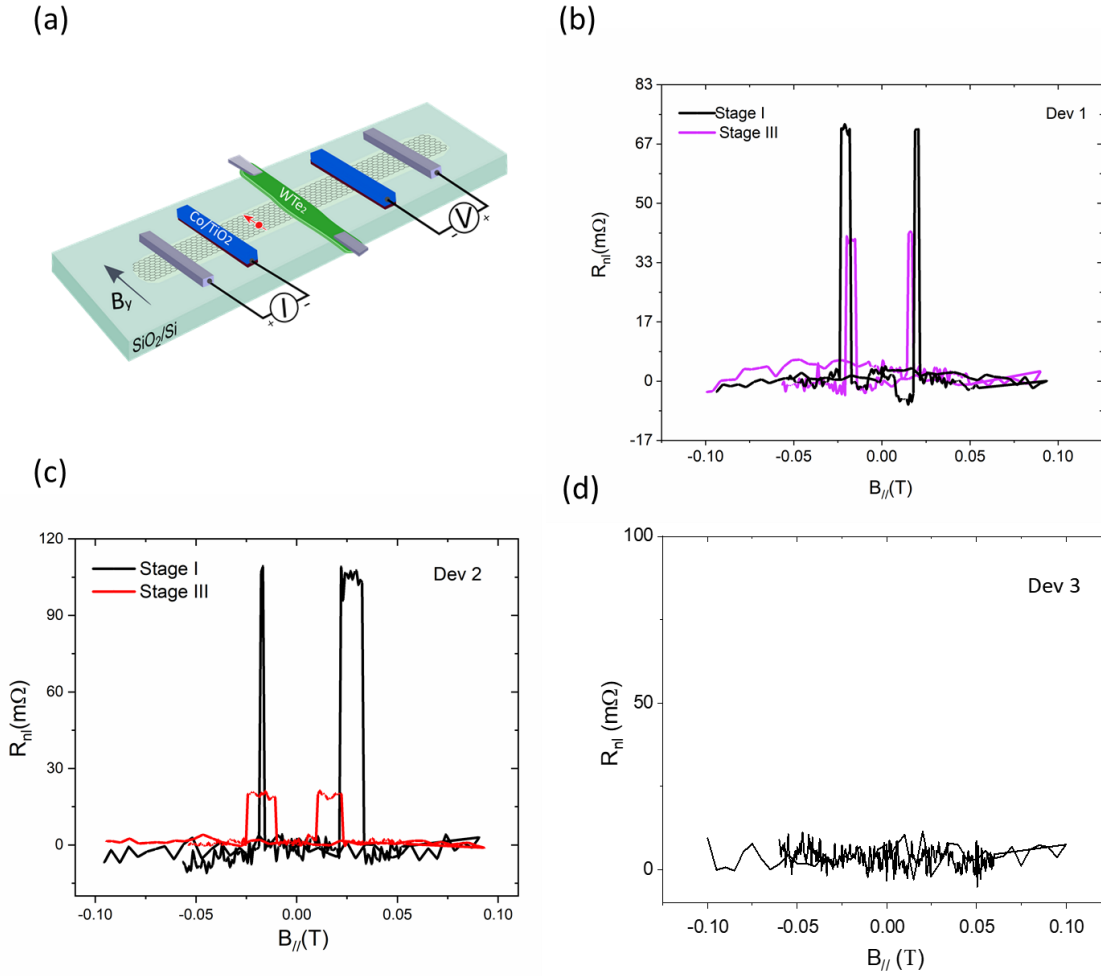


Figure S9. Spin absorption at the graphene-WTe₂ interface. (a) The spin-valve measurement geometry and the signal measured in the graphene channel in the heterostructure with WTe₂. (b,c) Due to the change of WTe₂-graphene interface resistances from stages-I to -III, we observed the large reduction of spin signal R_{nl} in Dev 1 and 2. (d) No spin signal was observed in the noise level across the heterostructure in Dev 3. To be noted, all the spin valve signals are measured at negative bias currents and the $R_{nl}=V_{nl}/I$, where I is the absolute value of the bias current magnitude.

Note 2. Estimation of the Spin Hall Angle and Spin Diffusion Length in

WTe₂

The calculation of shunting factor x is very crucial^{2,5} for (I)SHE measurement and for the verification of the possible SHE origins. The shunting factor is defined as the relative value under the assumption that all the charge current flows within WTe₂, while (1-x) means the corresponding current shunted by graphene. We use the 3D COMSOL AC/DC module to calculate current distribution in our WTe₂-graphene heterostructure with all the parameters taken from the devices. Our calculation result shows that the shunting effect is highly suppressed due to the relatively higher interface resistance of WTe₂-graphene and the comparable conductivity of the two materials. Therefore, the shunting factor $x \approx 1$. Therefore, all the shunting related origins can be ruled out, such as proximity-induced SHE in graphene and proximity induced Rashba-Edelstein effect in graphene^{6,7}.

To estimate the spin Hall angle θ_{SH} and spin diffusion length λ_{WTe2} in WTe₂, usually one should obtain the spin diffusion length from spin absorption experiments^{2,8}, in which one can estimate the spin diffusion length from the reduction of spin signal due to the presence of WTe₂ in the graphene channel. However, experimentally it is challenging to compare different graphene spintronic devices with and without WTe₂, as FM contact spin polarization, tunnel resistances and graphene spin transport parameters and channel doping level are not always comparable in the device with and without the WTe₂ layer. These factors can affect the magnitude of the spin signals and spin lifetime in the channels. So, it is not reliable to obtain the λ_{WTe2} by the spin absorption experiments. Therefore, here we use both the in-plane ISHE^{2,8} and out-of-plane ISHE⁹ method in the same device (Dev 3) for estimation of spin parameters. By comparing the results from these two methods, we can check the self-consistency and reliability of the calculations.

Out-of-plane ISHE - For the out-of-plane ISHE, we adopt the formula as below⁹,

$$R_{ISHE}(B_z) = \frac{p_i \theta_{SH} \rho_M L_{SH} \lambda_{WTe2}}{w_M t_M} \left[\frac{1 - \exp(-\frac{t_M}{\lambda_{WTe2}})}{1 + \exp(-\frac{t_M}{\lambda_{WTe2}})} \right] \int_0^\infty \frac{\exp(-\frac{L_{SH}^2}{4D_s t})}{t \sqrt{4\pi D_s t}} \sin(\omega_0 B_z t) \exp(-\frac{t}{\tau_s}) dt, \quad S(1)$$

Where ρ_M , w_M , t_M , θ_{SH} and λ_{WTe2} are resistivity, width, thickness, spin Hall angle and spin diffusion length of WTe₂, respectively. L_{SH} is graphene channel length, $p_i=0.32$ and $D_s=0.032\text{m}^2/\text{s}$ are the effective spin polarization of Co/TiO₂ and spin diffusion constant which are extracted from the standard Hanle fitting of the spin valve nearby the WTe₂. Here we assume the D_s does not change in all the graphene area. τ_s is the spin diffusion time in graphene. $\omega_0 = g\mu_B/\hbar$ is the Larmor precession frequency, where $g=2$ is Lande g -factor, μ_B and \hbar are the Bohr magneton and reduced Planck constant. If the $\theta_{SH}=0.013$ is taken from the literature¹⁰, one can extract that the $\lambda_{WTe2} = 8 \pm 0.9\text{nm}$ and $\tau_s = 185 \pm 9\text{ps}$ (main text Fig.2c) from the Eq. S1

fitting. The spin resistance $R_{s,WTe2} = \frac{\rho_M \lambda_{WTe2}}{w_M w_{gr} \tanh(t_M/\lambda_{WTe2})} \approx 80\text{m}\Omega \ll R_{s,gr} = \frac{R_{sq,gr} \lambda_{gr}}{w_{gr}} \approx 1.2\text{k}\Omega$ which is vital to

guarantee the accurate extraction for the shunting effect can be highly suppressed⁹.

In-plane ISHE - In order to quantitatively understand the in-plane ISHE data from the same device, we use a model based on one-dimensional spin diffusion equations. The detected ΔR_{ISHE} can be expressed as^{2,11,12}:

$$\Delta R_{ISHE} = \frac{2\theta_{SH} \rho_M x}{w_M} \left(\frac{\hat{I}_s}{I_c} \right) \quad S(2)$$

Where x is the shunting factor. The effective spin current \hat{I}_s injected vertically from graphene into the WTe₂ results in a charge current of I_c . Where,

$$\frac{\hat{I}_S}{I_c} \equiv \frac{\int_0^{t_M} I_S(z) dz}{I_c \lambda_{WTe2}} = \frac{\lambda_{WTe2} (1 - e^{-\frac{t_M}{\lambda_{WTe2}}})^2 I_S(z=0)}{t_M (1 - e^{-2\frac{t_M}{\lambda_{WTe2}}}) I_c} \quad (S3)$$

$$= \frac{\lambda_M (1 - e^{-\frac{t_M}{\lambda_{WTe2}}})^2}{t_M (1 - e^{-2\frac{t_M}{\lambda_{WTe2}}})} \frac{2p_i Q_{IF1} [(2Q_{IF2} + 1)(1 - Q_{IM}) e^{-\frac{-L_{SH}}{\lambda_{gr}}} - (1 + Q_{IM}) e^{-\frac{-3L_{SH}}{2\lambda_{gr}}}]}{(2Q_{IF1} + 1)(2Q_{IF2} + 1)(1 + Q_{IM}) - (2Q_{IF1} + 1)(1 + Q_{IM}) e^{-\frac{-3L_{SHE}}{2\lambda_{gr}}} - (2Q_{IF2} + 1)(1 - Q_{IM}) e^{-\frac{-L_{SH}}{\lambda_{gr}}} - (Q_{IM} - 1) e^{-\frac{-2L_{SH}}{\lambda_{gr}}}}$$

Where $R_{gr} = \frac{R_{gr}^{\square} \lambda_{gr}}{w_{gr}}$, $Q_{IFi} = \frac{1}{1 - p^2} \frac{R_{ci}}{R_{gr}}$, with $i=1, 2$, R_{ci} corresponding to injector and detector contact resistance, respectively. $Q_{IM} = \frac{w_{gr} R_{cM}}{R_{gr}^{\square} \lambda_{gr}}$, R_{cM} , w_{gr} , R_{gr}^{\square} are WTe₂-graphene interface resistance, graphene channel width and square resistance, respectively. By analyzing the Eq. S2 and substituting all the device parameters from Dev 3 (Table 1 and Fig. S6), one can obtain the plot of the relation between the spin Hall angle $\theta_{(I)SHE}$ and spin diffusion length λ_{WTe2} (Fig.S10). As expected, by substituting $\lambda_{WTe2} = 8 \pm 0.9 \text{ nm}$ from the out-of-plane ISHE result, one obtains $\theta_{SH} = 0.014$, which is comparable to the value in the literature¹⁰ and proves the self-consistency in the calculations.

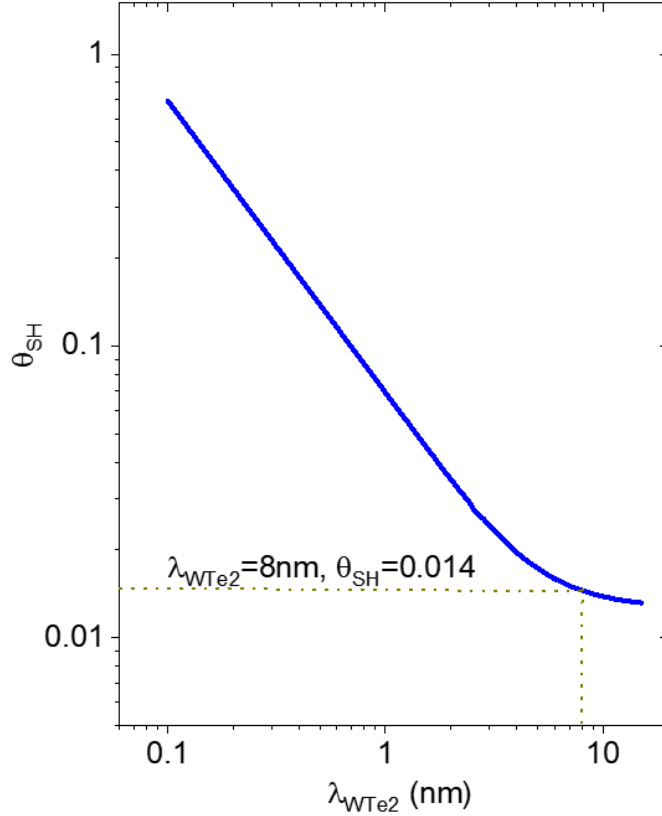


Figure S10. Estimation of spin Hall angle and spin diffusion length of WTe₂. Calculated spin parameters (λ_{WTe2} , θ_{SH}) in WTe₂ using a numerical solution to the Eq. S2 and parameters from Dev 3. The plot is the relation between spin Hall angle θ_{SH} and spin diffusion length λ_{WTe2} . The dashed lines show one possible solution.

References

- (1) Kim, Y.; Jhon, Y. I.; Park, J.; Kim, J. H.; Lee, S.; Jhon, Y. M. Anomalous Raman Scattering and Lattice Dynamics in Mono- and Few-Layer WTe₂. *Nanoscale* **2016**, *8* (4), 2309–2316.
- (2) Niimi, Y.; Morota, M.; Wei, D. H.; Deranlot, C.; Basletic, M.; Hamzic, A.; Fert, A.; Otani, Y. Extrinsic Spin Hall Effect Induced by Iridium Impurities in Copper. *Phys. Rev. Lett.* **2011**, *106* (12), 126601.
- (3) Dankert, A.; Dash, S. P. Electrical Gate Control of Spin Current in van Der Waals Heterostructures at Room Temperature. *Nat. Commun.* **2017**, *8* (May), 16093.
- (4) Yan, W.; Txoperena, O.; Llopis, R.; Dery, H.; Hueso, L. E.; Casanova, F. A Two-Dimensional Spin Field-Effect Switch. *Nat. Commun.* **2016**, *7*, 13372.
- (5) Liu, L.; Buhrman, R. A.; Ralph, D. C. Review and Analysis of Measurements of the Spin Hall Effect in Platinum. *arXiv Prepr. arXiv1111.3702* **2011**.
- (6) Ghiasi, T. S.; Kaverzin, A. A.; Blah, P. J.; van Wees, B. J. Charge-to-Spin Conversion by the Rashba-Edelstein Effect in 2D van Der Waals Heterostructures up to Room Temperature. **2019**, arXiv preprint arXiv:1905.01371.
- (7) Safeer, C. K.; Ingla-Aynés, J.; Herling, F.; Garcia, J. H.; Vila, M.; Ontoso, N.; Calvo, M. R.; Roche, S.; Hueso, L. E.; Casanova, F. Room-Temperature Spin Hall Effect in Graphene/MoS₂ van Der Waals Heterostructures. *Nano Lett.* **2019**, *19* (2), 1074–1082.
- (8) Yan, W.; Sagasta, E.; Ribeiro, M.; Niimi, Y.; Hueso, L. E.; Casanova, F. Large Room Temperature Spin-to-Charge Conversion Signals in a Few-Layer Graphene/Pt Lateral Heterostructure. *Nat. Commun.* **2017**, *8* (1), 661.
- (9) Savero Torres, W.; Sierra, J. F.; Benítez, L. A.; Bonell, F.; Costache, M. V.; Valenzuela, S. O. Spin Precession and Spin Hall Effect in Monolayer Graphene/Pt Nanostructures. *2D Mater.* **2017**, *4* (4), 041008.
- (10) MacNeill, D.; Stiehl, G. M.; Guimaraes, M. H. D.; Buhrman, R. A.; Park, J.; Ralph, D. C. Control of Spin-Orbit Torques through Crystal Symmetry in WTe₂/Ferromagnet Bilayers. *Nat. Phys.* **2017**, *13* (3), 300–305.
- (11) Sagasta, E.; Omori, Y.; Isasa, M.; Gradhand, M.; Hueso, L. E.; Niimi, Y.; Otani, Y.; Casanova, F. Tuning the Spin Hall Effect of Pt from the Moderately Dirty to the Superclean Regime. *Phys. Rev. B* **2016**, *94* (6), 060412.
- (12) Fujiwara, K.; Fukuma, Y.; Matsuno, J.; Idzuchi, H.; Niimi, Y.; Otani, Y.; Takagi, H. 5d Iridium Oxide as a Material for Spin-Current Detection. *Nat. Commun.* **2013**, *4* (1), 2893.